ChemPubSoc Europe

DOI: 10.1002/celc.201600236

CHEMELECTROCHEM Articles

Special Issue

Study of Hydrogen Peroxide Reactions on Manganese Oxides as a Tool To Decode the Oxygen Reduction Reaction Mechanism

Anna S. Ryabova,[a, b] Antoine Bonnefont,*[c] Pavel Zagrebin,[b] Tiphaine Poux,[a, f] Robert Paria Sena,[d] Joke Hadermann,[d] Artem M. Abakumov,[e] Gwénaëlle Kéranguéven,[a] Sergey Y. Istomin,[b] Evgeny V. Antipov,[b] Galina A. Tsirlina,[b] and Elena R. Savinova[a]

Hydrogen peroxide has been detected as a reaction intermediate in the electrochemical oxygen reduction reaction (ORR) on transition-metal oxides and other electrode materials. In this work, we studied the electrocatalytic and catalytic reactions of hydrogen peroxide on a set of Mn oxides, Mn_2O_3, MnOOH, $LaMnO_3$, MnO_2, and Mn_3O_4, that adopt different crystal structures to shed light on the mechanism of the ORR on these materials. We then combined experiment with kinetic modeling with the objective to correlate the differences in the ORR activity to the kinetics of the elementary reaction steps, and we uncovered the importance of structural and compositional factors in the catalytic activity of the Mn oxides. We concluded that the exceptional activity of Mn_2O_3 in the ORR is due to its high catalytic activity both in the reduction of oxygen to hydrogen peroxide and in the decomposition of the latter, and furthermore, we proposed a tentative link between crystal structure and reactivity.

1. Introduction

The reduction of oxygen into water is a key process for many energy-conversion devices, including fuel cells, metal–air batteries, and regenerative fuel cells.[1–3] However, the design of efficient and selective catalysts for the oxygen reduction reaction (ORR) remains a major challenge. The ORR follows a complex multielectron-transfer mechanism that involves the formation of several intermediates, which results in sluggish reaction kinetics and high reaction overpotential.[4]

Recently, the study of the ORR in alkaline media has attracted renewed attention stimulated by the development of novel anion-exchange membranes[5] and inspired by the possibility of using noble-metal-free catalysts.[6,7] Within this context, manganese oxides are considered as promising catalysts for the reduction of oxygen at the cathode of alkaline fuel cells, as they combine low cost, environmental friendliness, and fair activities in the ORR in comparison to state-of-the-art noble-metal-based catalysts.[8] However, despite numerous studies on Mn oxides, the reaction mechanism and the main factors influencing the ORR activity on such catalysts are not yet fully understood. In alkaline media, the overall oxygen reduction reaction into water is [Eq. (1)]:

$$O_2 + 2\,H_2O + 4\,e^- \rightleftharpoons 4\,OH^-$$
$$E^\circ = 1.23\,V \text{ vs. RHE} \quad \text{at pH } 14 \qquad (1)$$

On several electrode materials, including transition-metal oxides, hydrogen peroxide has been identified as a stable intermediate of the ORR.[9–12] On such electrodes, the reduction of oxygen into water occurs through a "series" $2\,e^- + 2\,e^-$ pathway with intermediate hydrogen peroxide formation, which, depending on the pH, may be present in solution in either the H_2O_2 or HO_2^- form [$pK_a(H_2O_2) = 11.7$] [Eq. (2)]:[13]

$$O_2 + H_2O + 2\,e^- \rightleftharpoons HO_2^- + OH^-$$
$$E^\circ = 0.77\,V \text{ vs. RHE} \quad \text{at pH } 14 \qquad (2)$$

[a] A. S. Ryabova, Dr. T. Poux, Dr. G. Kéranguéven, Prof. E. R. Savinova
ICPEES, UMR 7515 CNRS-ECPM, Université de Strasbourg
25, rue Becquerel, 67087 Strasbourg Cedex 2 (France)

[b] A. S. Ryabova, Dr. P. Zagrebin, Dr. S. Y. Istomin, Prof. E. V. Antipov, Prof. G. A. Tsirlina
Moscow State University
Leninskie Gory, 1-str. 3, Moscow 119991 (Russia)

[c] Dr. A. Bonnefont
IC, UMR 7177, CNRS, Université de Strasbourg
4 rue Blaise Pascal, 67000 Strasbourg (France)
E-mail: bonnefont@unistra.fr

[d] R. Paria Sena, Prof. J. Hadermann
EMAT, University of Antwerp, Department of Physics
Groenenborgerlaan 171, 2020 Antwerp (Belgium)

[e] Prof. A. M. Abakumov
Center for Electrochemical Energy Storage
Skolkovo Innovation Center
3 Nobel Street, Moscow 143026 (Russia)

[f] Dr. T. Poux
Current address:
Paul Scherrer Institute
5232 Villigen PSI (Switzerland)

Supporting Information for this article can be found under http://dx.doi.org/10.1002/celc.201600236.

Special Issue

Invited contribution to a Special Issue on Electrocatalytic Nanomaterials

followed by the reduction of HO_2^- [Eq. (3)]:

$$HO_2^- + H_2O + 2e^- \rightleftharpoons 3\,OH^-$$
$$E^\circ = 1.71\,V \text{ vs. RHE} \quad \text{at pH } 14 \tag{3}$$

Note that H_2O_2 can also decompose in a chemical reaction, which, depending on the solution pH, may be expressed as follows [Eqs. (4) and (5)]:

$$H_2O_2 \rightarrow H_2O + {}^1/_2\,O_2 \tag{4}$$

$$HO_2^- \rightarrow OH^- + {}^1/_2\,O_2 \tag{5}$$

Clearly, the reactions shown in Equations (1)–(5) are not elementary and consist of several chemical and electrochemical steps. Such a "series" $2e^- + 2e^-$ ORR pathway with the intermediate formation of hydrogen peroxide was recently confirmed for manganese and cobalt oxides with the perovskite structure.[14] Given that the reaction of Equation (3) is the reduction of hydrogen peroxide and that Equation (−2) is the oxidation of HO_2^- into O_2, investigation of the kinetics of the electrochemical reactions of hydrogen peroxide is complementary to the ORR study (e.g. see Ref. [15]). Therefore, concurrent analysis of the experimental data for the ORR and the hydrogen peroxide oxidation/reduction reactions for a set of well-defined catalysts is expected to provide further information on the mechanism of the ORR and on the kinetics of the reaction steps and their dependence on the structure and composition of the catalyst.

Recently,[16] we performed a combined experimental and microkinetic modeling study of the ORR for a series of binary and complex manganese oxides. The ORR activity was found to depend strongly on their structure, and Mn_2O_3 exhibited the highest activity. It was demonstrated that the specific activity of Mn oxides was correlated with the formal potential of the $Mn^{IV/III}$ redox transition (E_f), which suggested the latter as a descriptor for the ORR electrocatalysis. Note that E_f is directly related to the Gibbs free-energy difference for surface adsorbates O_{ad} and OH_{ad} (see the scheme presented in Figure 1).

To further the understanding of the ORR mechanism, in this work we study the reaction pathways for the same series of manganese oxides, Mn_2O_3, MnOOH, $LaMnO_3$, MnO_2, and Mn_3O_4, adopting different crystal structures. We apply the rotating disc electrode (RDE) to compare the kinetics of the ORR and the hydrogen peroxide oxidation/reduction reactions (HPOR/HPRR) and also address the kinetics of the catalytic decomposition of hydrogen peroxide [Eqs. (4) and (5)] on these Mn oxides. Then, the experimental data are analyzed with the help of a kinetic model based on the reaction scheme proposed in our earlier publications[14–16] and displayed in Figure 1. The kinetic model takes into account the (electro)chemical kinetics of a set of elementary reaction steps involved in the oxygen and hydrogen peroxide reactions and the mass transport of the reactants, intermediate species, and products to (from) the electrode surface. This model was able to account for the ORR and HPOR/HPRR on perovskite-type oxides.[14,15] Recently, we applied it to the analysis of the RDE data for the ORR on various Mn oxides,[16] whereby the model was capable of explaining the influence of the $Mn^{IV/III}$ redox potential on the ORR activity.

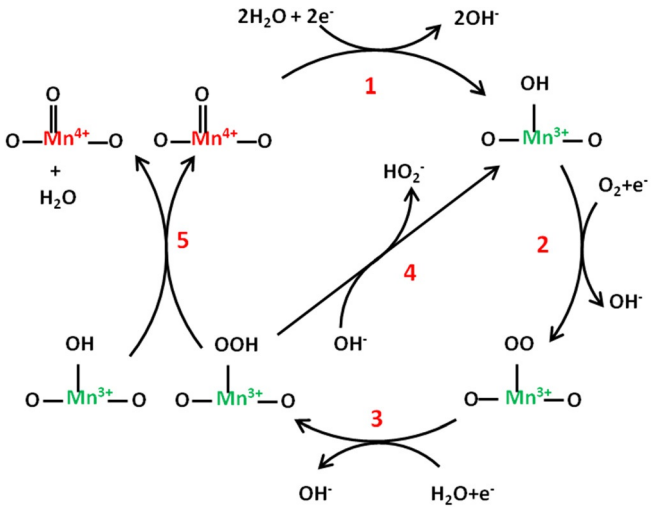

Figure 1. Tentative mechanism for the oxygen reduction/hydrogen peroxide reactions. Steps 1/−1 are the conversion of adsorbed O_{ad}/OH_{ad} accompanied by Mn^{IV}/Mn^{III} redox transition ($Mn^{IV}=O/Mn^{III}$-OH) of surface cations. Steps 2/−2 are electrochemical O_2 adsorption/desorption, which occur by displacement of adsorbed OH species accompanied by electron transfer and can only occur on/from Mn^{III} sites (green). Steps 3/−3 are coupled electron and proton (from water molecule) transfer. Steps 4/−4 are adsorption/desorption of HO_2^-. Step 5 is a chemical step involving dissociation of the O–O bond, which results in the formation of two Mn^{IV} sites (red). Reproduced with permission from Ref. [16].

In this work, we consider three independent experimental data sets: 1) the RDE data for the ORR, 2) the RDE data for the HPRR/HPOR, and 3) the kinetics of the catalytic decomposition of hydrogen peroxide. For each manganese oxide considered in this work, the parameters of the kinetic model are adjusted to reproduce semiquantitatively the main features of the three sets of experimental data to find out which kinetic parameters, beyond the formal potential of the $Mn^{IV/III}$ redox transition (E_f), affect the ORR kinetics on Mn oxides. Using this approach, significant differences in the ORR activity in the set of Mn oxides can be correlated to strong differences in the kinetics of the elementary reaction steps, shedding light on the importance of structural and compositional factors in the ORR activity of Mn oxides.

Experimental and Modeling Details

Synthesis and Characterization of Mn oxides

The syntheses of the Mn_2O_3, MnO_2, MnOOH, Mn_3O_4, $LaMnO_3$, and $La_{0.8}Sr_{0.2}MnO_3$ oxides, as well as their characterization by X-ray powder diffraction, scanning electron microscopy, and nitrogen adsorption (following multiple-point BET method) are documented in Ref. [16]. The structural and morphological characteristics of the Mn oxides are summarized in Table 1.

High angular annular dark field scanning transmission electron microscopy (HAADF-STEM) images were taken with a FEI Titan transmission electron microscope with probe and image aberration cor-

Table 1. Structural and morphological characteristics of Mn oxides.

Entry	Sample notation	Main phase (structure type)	BET area [$m^2 g^{-1}$]
1	Mn_2O_3_wet_3[a]	α-Mn_2O_3 (bixbyite)	27
2	Mn_2O_3_milled[a]	α-Mn_2O_3 (bixbyite)	8
3	Mn_2O_3_wet_1[a]	α-Mn_2O_3 (bixbyite)	3
4	$LaMnO_3$	$LaMnO_3$ (perovskite)	14
5	$La_{0.8}Sr_{0.2}MnO_3$	$La_{0.8}Sr_{0.2}MnO_3$ (perovskite)	18
6	MnO_2	β-MnO_2 (pyrolusite)	48
7	MnOOH	α-MnOOH (manganite)	55
8	Mn_3O_4	Mn_3O_4 (hausmannite)	13
9	Sibunit carbon		66

[a] Three samples of Mn_2O_3 prepared with various synthetic procedures (as detailed in Ref. [16]) were utilized in this work. Briefly, the Mn_2O_3_wet_1 sample was obtained by spray pyrolysis at 800–900 °C of an aerosol produced from 0.3 M $Mn(CH_3COO)_2$ aqueous solution, whereas Mn_2O_3_wet_3 was prepared by calcination in air at 500 °C of the co-proportionation product of $Mn(CH_3COO)_2$ and $KMnO_4$. The Mn_2O_3_milled sample was obtained by ball milling of commercially available Mn_2O_3 ("Reachim", Russia). The Mn_2O_3_wet_3 sample was used for electrochemical measurements, as its larger specific surface area was suitable for precise evaluation of the electrocatalytic activity. In contrast, the Mn_2O_3_wet_1 and Mn_2O_3_milled samples were prepared in large quantities and were used in the H_2O_2 decomposition studies, which required larger amounts of catalysts. Note, however, that according to our previous work,[16] the specific (surface weighted) activities of these Mn_2O_3 oxide samples in the ORR are the same.

rectors. The samples for transmission electron microscopy (TEM) were prepared by crushing powder with an agate mortar and pestle, dispersing the crushed powder in ethanol, and depositing a few drops of this suspension on a copper grid covered with a holey carbon film.

Electrode Preparation

Thin films of oxide/carbon (1:1 mass) composites[17] were deposited on a glassy carbon (GC) rod (0.07 cm^2 geometric area) of an Autolab RDE, which was mechanically polished to a mirror finish by using alumina paste (down to 0.05 μm). The geometric surface area of the GC is denoted below by the subscript "geo". The oxide/carbon ratio was chosen to minimize the ohmic resistance of the catalyst film.[16,17] Carbon of the Sibunit family[18] with a BET surface area of 65.7 $m^2 g^{-1}$ was chosen for its high purity and high electronic conductivity. To improve the oxide/carbon contact, required amounts of carbon and oxide were ground in a mortar, and then a desired sample dose was mixed with ultrapure water (18.2 MΩ cm, <3 ppb TOC, Purelab) to prepare an ink, which was ultrasonicated for 30 min, drop cast onto the GC support, and dried under an atmosphere of N_2. After drying, the alkaline ionomer AS-4 (2 μL) from the Tokuyama Company (8.68 μL AS-4 in 4 mL H_2O) was deposited on top of the layer and dried under an atmosphere of N_2. If not otherwise stated, the loading was 91 $\mu g\,cm^{-2}_{geo}$ both for the oxide and for carbon. Pt/C (40 wt% Pt on carbon black, Alfa Aesar) was used for benchmarking.

Electrochemical Characterization

Electrochemical measurements were performed in a standard three-electrode cell. All parts of the electrochemical cell in contact with the alkaline electrolyte were from Teflon, and the remaining parts were from Pyrex glass. 1 M NaOH electrolyte was prepared from an extrapure NaOH solution (Acros Organics, 50 wt% solution in water) and Milli-Q water (Purelab: 18.2 MΩ cm, <3 ppb TOC). The working electrode was a RDE, as described above. The counter electrode was a Pt wire, and the reference electrode was a Hg/HgO/1 M NaOH electrode (+0.93 V vs. RHE). Here and below all potentials E are referred to the RHE. The electrolyte resistance determined from the high-frequency part of the electrochemical impedance spectra (measured in the 1 Hz to 100 kHz range) was equal to about 15 Ω. RDE curves were corrected to the ohmic drop. Electrochemical measurements were performed by using an Autolab potentiostat with an analog scan generator at a scan rate of 10 $mV s^{-1}$ at 25 °C.

Cyclic voltammograms were obtained in N_2-purged electrolyte within a stability potential window determined for each compound individually. H_2O_2 solutions were prepared from 30 wt% solution in water (SupraPur, Merck), and before using, H_2O_2 was titrated with standardized $KMnO_4$. RDE voltammograms were obtained in O_2-saturated electrolyte and N_2-purged electrolyte with 0.42–6.72 mM of H_2O_2 under rotation rates of 400–2500 rpm at a 10 $mV s^{-1}$ scan rate. Voltammetric tests demonstrated satisfactory stability of oxides in peroxide-containing media (see Figure S1.1 in the Supporting Information for details).

Catalytic Hydrogen Peroxide Decomposition

The kinetics of the catalytic HO_2^- decomposition were investigated in a large-volume (920 mL) Pyrex batch reactor filled with O_2-saturated Milli-Q water and containing a desired amount of a suspended milled catalyst in a thermostatically controlled setup [$T=(25\pm0.5)$ °C] similar to that described in refs. [19,20]. For further details, see the Supporting Information (Section S2.1). The decomposition kinetics of H_2O_2 were monitored by measuring the volume of O_2 evolved after the injection of a H_2O_2 dose required to achieve 0.99 mM concentration in the reactor. The concentration of H_2O_2 was determined by titration with a $KMnO_4$ solution in the presence of 1 M sulfuric acid. The data were collected for different loadings of each catalyst to obtain reliable rate constants. For each loading, the results of three experiments were averaged. Complementary experiments were performed for selected Mn oxides in a 1 M NaOH solution containing hydrogen peroxide. The details can be found in the Supporting Information (Section S2.2).

Microkinetic Modeling

The observed experimental differences between various manganese oxides in the ORR and in the HPOR/HPRR were rationalized with the help of a microkinetic model. Kinetic constants of the reaction steps (see Figure 1) were varied until the model was able to reproduce the main features of the three sets of experimental data (with the same set of equations and kinetics parameters), namely, the 1) RDE curves for the ORR, 2) the RDE curves for the HPRR/HPOR, and 3) the heterogeneous rate constant for hydrogen peroxide decomposition. For the reactions occurring on Mn oxides, the scheme displayed in Figure 1 comprises the elementary reaction steps involved in the mechanisms of both the O_2 and HO_2^- reactions. The Mn^{IV}/Mn^{III} redox transition at the Mn oxide surface is considered in step 1, for which the O_{ad} and OH_{ad} species are assumed to be coordinated to the Mn^{IV} and Mn^{III} surface cations, respectively. Steps 2 and 3 correspond to the reduction of O_2 into adsorbed HO_2^-, whereas backward steps −3 and −2 represent the oxidation of adsorbed HO_2^- into O_2. The reduction of adsorbed

HO_2^- occurs through an irreversible chemical surface process, in which the O–O bond is broken (see step 5), followed by step 1. Finally, steps 4 and −4 correspond to the desorption/adsorption of HO_2^- from/on the Mn^{III} site. This reaction scheme is also able to account for the catalytic decomposition of HO_2^- at the open-circuit potential in a concurrent HPOR (responsible for the transformation of HO_2^- into O_2) and HPRR (transformation of HO_2^- into H_2O). Simulation of the current potential curves for the ORR and HPOR/HPRR were performed under steady-state conditions by assuming a linear concentration profile of O_2 or HO_2^- in the diffusion layer. A flat catalyst layer on which carbon and Mn oxides were perfectly mixed was also assumed so that the concentration of O_2 or HO_2^- was the same in the vicinity of the active Mn oxide or carbon sites. Calculation of the heterogeneous rate constant (k_{het}) for HO_2^- decomposition was performed under the assumption of kinetic control if the reaction rate was not influenced by mass transfer of either O_2 or HO_2^-.

As the ORR and the electrochemical HPRR/HPOR were studied by using Mn oxide/carbon composite electrodes, the reduction of O_2 into HO_2^- on carbon was also included in the kinetic model. According to our previous studies, the reduction of oxygen into HO_2^- on carbon in the composite electrodes can be well described by a simple mechanism by taking into account the adsorption of oxygen [Eq. (6)], its electrochemical reduction into $HO_2^-{}_{,ad}$ [Eq. (7)], and desorption of the latter from the surface of carbon (step −8) [Eq. (8)]:

$$O_2 + * \rightleftharpoons O_{2,ad} \quad (6)$$

$$O_{2,ad} + H_2O + 2e^- \rightleftharpoons HO_2^-{}_{,ad} + OH^- \quad (7)$$

$$HO_2^- + * \rightleftharpoons HO_2^-{}_{,ad} \quad (8)$$

in which * is a free site on the carbon surface. Further details on the kinetic model as well as the kinetic equations can be found in the Supporting Information (Section S3).

2. Results and Discussion

2.1. High Angle Annular Dark Field STEM

Figure 2 presents the HAADF-STEM images of the different materials. Low-magnification overview images showing a larger set of crystals are shown in Figure S4.1. All samples consist of nanometer-sized oxide particles. MnOOH and MnO_2 both show the presence of different types of particles (Figure S4.1), including rodlike particles that can have a length of several hundred nanometers and small particles (10–50 nm). In MnO_2, all types of particles are nicely facetted, whereas in MnOOH there is a higher frequency of irregular faces, both for the small particles and for the ends of the rod-shaped particles. The sides of the rod-shaped particles in MnOOH also sometimes have a corrugated appearance. Mn_2O_3 shows round-shaped particles at low magnification, which in the high-resolution HAADF-STEM images appear faceted with dominating straight facets confined to the {111} crystal planes of the cubic bixbyite structure. The shapes of the particles in Mn_3O_4 and $LaMnO_3$ are random, and no clear crystal faces are formed. In Mn_2O_3, Mn_3O_4, and $LaMnO_3$, the range of sizes varies from several tens of nanometers to several hundreds of nanometers.

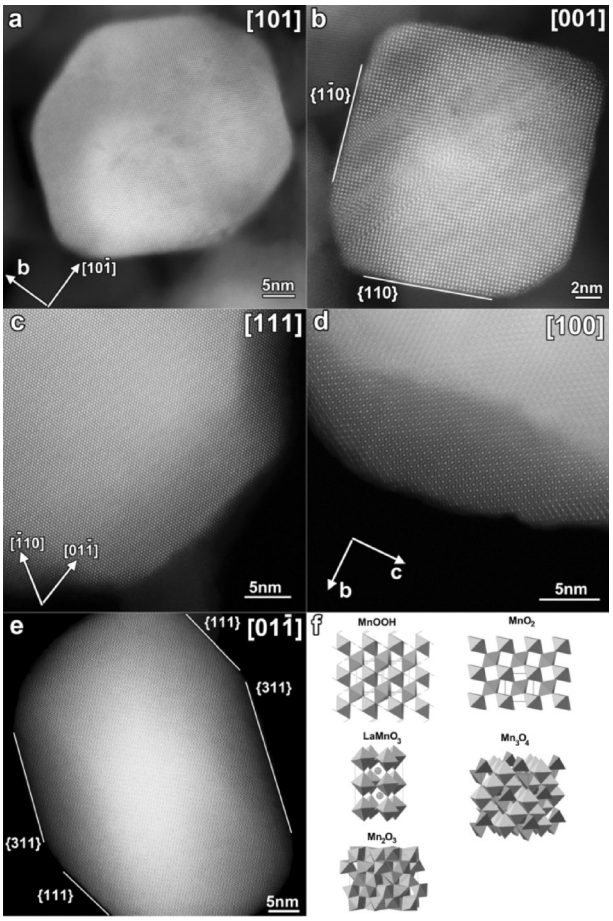

Figure 2. High-resolution HAADF-STEM images of a) MnOOH, b) MnO_2, c) $LaMnO_3$, d) Mn_3O_4, and e) Mn_2O_3. Models of the different structures are given in the same order in panel (f).

2.2. RDE Study of the Electrochemical Reactions of Hydrogen Peroxide

2.2.1. Rotation Rate Dependence

The positive scans of the RDE current–potential (*j*–*E*) curves measured for oxide/carbon composite electrodes in alkaline hydrogen peroxide solution are displayed in Figure 3 for various rotation rates. For the sake of comparison with the ORR RDE voltammograms (see Section 2.4.), the concentration of hydrogen peroxide (0.84 mM) was set to a value similar to that of O_2 in a saturated 1 M NaOH electrolyte. In the absence of Mn oxides, the HPOR and HPRR currents were small (see voltammograms acquired for carbon film electrodes in Figure S5.1), which confirms that the measured current is mainly due to the HPRR/HPOR electrocatalysis on Mn oxides.

The measured RDE curves result from the interplay of three reactions: the anodic current stems from the HPOR [Eq. (−2)], whereas the cathodic current is the sum of the HPRR [Eq. (3)] and the reduction of O_2 [Eqs. (1) and/or (2)] locally produced by the HPOR at the surface of the electrode, although the bulk of the solution is free of O_2 due to efficient N_2 purging. Note that the anodic contribution of the oxidation of OH^- to HO_2^- [Eq. (−3)] can be neglected in the studied potential range [see

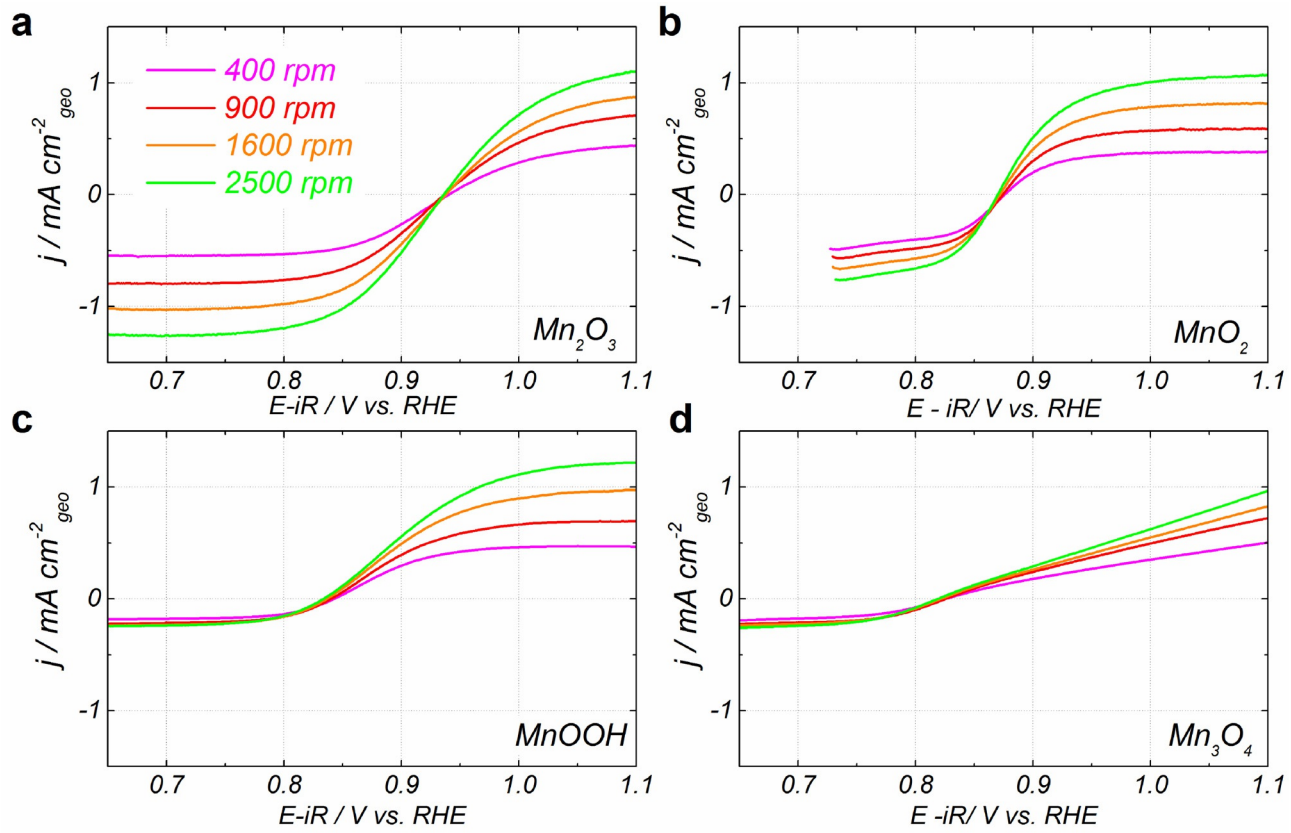

Figure 3. a) Positive scans of the RDE voltammograms in N_2-purged 1 M NaOH + 0.84 mM H_2O_2 at 10 mV s^{-1} for GC-supported thin films of a) Mn_2O_3_wet_3/C, b) MnO_2/C, c) MnOOH/C, and d) Mn_3O_4/C. Catalyst loadings are 91 μg cm^{-2} oxide + 91 μg cm^{-2} carbon. Color codes: 400 (magenta), 900 (red), 1600 (orange), 2500 rpm (green). Currents are normalized to the electrode geometric area and corrected to the background currents measured under the N_2 atmosphere. RDE voltammograms for $LaMnO_3$ are shown in Figure S5.2. For comparison of the positive and negative voltammetric scans, see Figure S5.3.

value of E° for Eq. (3)]. Under open-circuit conditions, the sum of the currents of these three reactions equals zero, and a mixed potential (E_{mix}) is established at the electrode. The value of E_{mix} is determined by the relative rates of the HPOR, HPRR, and ORR; the faster the kinetics for the HPOR relative to the sum of the kinetics for the HPRR and ORR, the more E_{mix} is shifted towards negative values, and vice versa. Comparison of the RDE curves displayed in Figure 3 reveals significant differences in the E_{mix} values and in the limiting anodic and cathodic currents for various Mn oxides (see the RDE curves for Pt/C and Mn perovskites in Ref. [15]). In what follows, we explain these differences by using a combination of experimental and modeling approaches.

The most striking difference between the Mn oxides emerging from Figure 3 comes to light in the dependence of the cathodic limiting currents on the rotation rate. Whereas for Mn_2O_3/C the absolute values of the cathodic limiting currents increase with the rotation rate, for Mn_3O_4/C and MnOOH/C they are virtually rotation rate independent. MnO_2/C demonstrates an intermediate case with rotation-rate dependent cathodic limiting currents, which, however, do not reach the value expected for a diffusion-limited 2e$^-$ reduction reaction (see Figure 3a for Mn_2O_3). At variance, the anodic limiting currents are reached for all samples except for Mn_3O_4.

To better visualize the rotation rate dependence, the limiting cathodic and anodic currents are displayed in the form of Levich–Koutecký (LK) plots in Figure 4. Whereas the LK plots for currents measured at a positive potential limit (1.1 V vs. RHE) for all samples (except for Mn_3O_4)[1] are the same (Mn_2O_3, $La_{0.8}Sr_{0.2}MnO_3$, MnOOH) or similar (MnO_2) to the one for Pt/C, which confirms that they are controlled by mass transport of HO_2^- to the electrode surface, the LK plots for the cathodic currents show three different behaviors. For the Mn_2O_3/C and $La_{0.8}Sr_{0.2}MnO_3$/C composites, the LK plots at 0.65 V versus RHE coincide with that of Pt/C, that is, they correspond to a mass-transport-controlled 2e$^-$ reduction reaction. For MnOOH/C and Mn_3O_4/C, the LK plots confirm rotation-rate independence of the cathodic limiting current, which suggests that at the specified potential the HO_2^- reduction current is not limited by diffusion but rather by a slow chemical step. Finally, the MnO_2/C composite at +0.75 V versus RHE is an intermediate case between Mn_2O_3/C or $La_{0.8}Sr_{0.2}MnO_3$/C and Mn_3O_4/C or MnOOH/C with a slope similar to that for the first group (Mn_2O_3 and $La_{0.8}Sr_{0.2}MnO_3$) but with a non-zero *y* axis origin, which sug-

[1] *We cannot exclude that the specific behavior of this material is related to its poorer stability under polarization in H_2O_2-containing solutions (see Figure S1.1).*

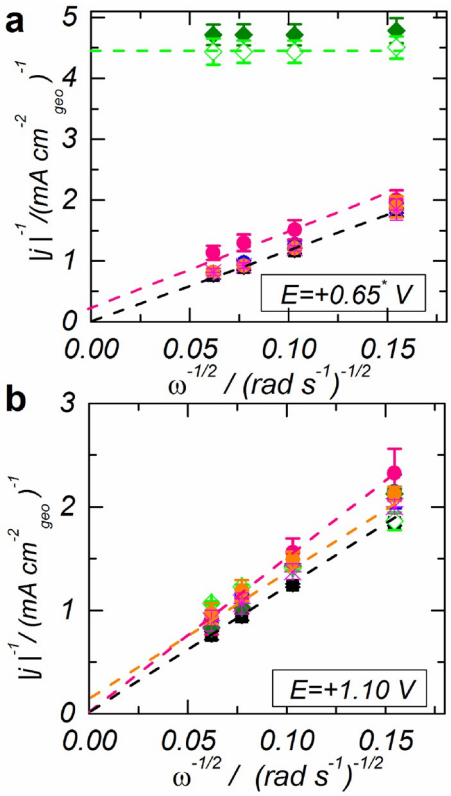

Figure 4. Levich–Koutecký (LK) plots of the a) cathodic (at +0.65 V_{RHE} for all samples except for MnO_2, for which the cathodic limit was restricted to 0.75 V_{RHE} to avoid sample degradation) and b) anodic (at +1.1 V_{RHE}) currents extracted from RDE voltammograms in N_2-purged 1 M NaOH + 0.84 mM H_2O_2 (Figures 3 and S5.2) for $LaMnO_3$/C (orange), $La_{0.8}Sr_{0.2}MnO_3$ (magenta), Mn_2O_3_wet_3/C (blue), MnO_2/C (pink), MnOOH/C (olive), and Mn_3O_4/C (green); ω: angular rotation rate. Error bars represent standard deviations from at least two independent measurements. Data for Pt/C (black) are replotted from Ref. [15] for comparison. The LK plots obtained for all Mn oxides at 0.75 V vs. RHE are displayed in Figure S5.5.

gests that the HPRR limiting current is under the mixed control of mass transport and the chemical step.

2.2.2. Influence of H_2O_2 Concentration

The influence of the concentration of HO_2^- on the kinetics of the electrochemical hydrogen peroxide reactions is displayed in Figure 5. The shape of the polarization curves remains qualitatively the same as the H_2O_2 concentration is increased. The anodic limiting current for all samples except for that of Mn_3O_4 increases linearly with the concentration following the first-order rate law, as expected for a diffusion-limited current (Figure S5.4). Meanwhile, the concentration dependence of the limiting cathodic current (Figure 6) for various oxide materials is not the same. Whereas for Mn_2O_3 and $La_{0.8}Sr_{0.2}MnO_3$ a first-order rate law is observed, for MnOOH and Mn_3O_4 the increase in the absolute value of the current with the concentration is marginal. This observation supports our conjecture that at high cathodic overpotentials the current for MnOOH and Mn_3O_4 is controlled by a surface chemical reaction. Meanwhile, MnO_2 is a borderline case between the two behaviors, which confirms the hypothesis that the cathodic limiting current is under the mixed control of mass transport and the chemical step. The value of E_{mix} for all studied manganese oxides shifts to more negative values with the H_2O_2 concentration (see insets in Figure 5) or with the rotation rate of the electrode (see Figure 3). Such shifts were also observed for oxides with the perovskite structure in Ref. [15] and indicate that concentration and mass transport differently affect the HPOR and HPRR.

2.3. Study of the Catalytic Decomposition of Hydrogen Peroxide

Hydrogen peroxide decomposes into H_2O and O_2 according to Equations (4)/(5). H_2O_2 decomposition catalyzed by transition-metal oxides, including perovskites,[21–27] is known to be a first-order reaction. This was confirmed for our Mn oxides in alkaline (see Section S2) and neutral media. Typical kinetic curves showing $\ln[1-V(O_2)/V(O_2)_{max}]$ versus time (t) plots [in which $V(O_2)_{max}$ is the maximum O_2 volume calculated by using the ideal gas law] are shown in Figure 7 and demonstrate satisfactory linearity in the interval from 0 up to about 70% H_2O_2 conversion. The slope of the linear interval was used to calculate the first-order rate constant (k) according to Equation (9):

$$\ln\left[\frac{1-V(O_2)}{V(O_2)_{max}}\right] = -kt \qquad (9)$$

Note that the noncatalytic decomposition of hydrogen peroxide was sufficiently slow under the employed experimental conditions and could be neglected (see Figure 7).

The heterogeneous rate constant (k_{het}) expressed in cm s^{-1} was calculated as follows [Eq. (10)]:

$$k_{het} = \frac{kV_S}{m_{cat}S_{BET}} \qquad (10)$$

in which V_s is volume of the H_2O_2 solution, m_{cat} is the mass of the catalyst, and S_{BET} is the BET surface area of the catalyst.

The values of k_{het} calculated by using Equation (10) from the experimental data for various Mn oxides are presented in Table 2 along with parameters determined from simulations, which will be discussed in Section 2.4. First, we note that all Mn oxides demonstrated noticeable catalytic activity in the decomposition of hydrogen peroxide in agreement with the literature data.[25–28] Nevertheless, significant differences in the catalytic activities of the Mn oxides for hydrogen peroxide decomposition were observed, and the catalytic activity varied in the order MnOOH < $LaMnO_3$ < MnO_2 < Mn_2O_3. In particular, remarkably high catalytic activity was observed for Mn_2O_3, and the heterogeneous rate constant for H_2O_2 decomposition was almost 10 times higher than that for MnO_2 and 50 times higher than that for MnOOH. Notably, the activity in the catalytic decomposition of H_2O_2 scales roughly the same way as the electrocatalytic activity in the ORR,[16] which confirms the importance of the H_2O_2 transformation reactions in the complex multistep ORR mechanism (see Figure 1). It is worth men-

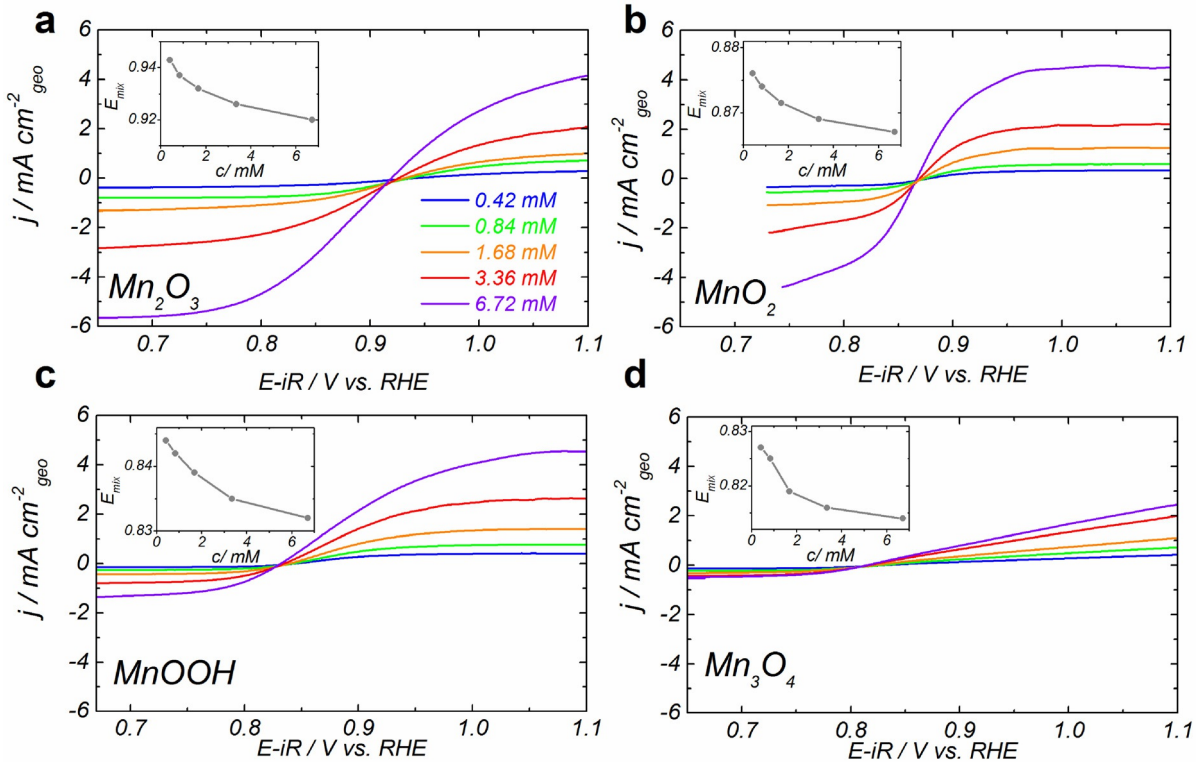

Figure 5. Positive scans of the RDE voltammograms in N_2-purged solutions of 1 M NaOH and various H_2O_2 concentrations at 900 rpm and 10 mV s^{-1} for GC-supported thin films of a) Mn_2O_3_wet_3/C, b) MnO_2/C, c) MnOOH/C, and d) Mn_3O_4/C. Catalyst loadings were 91 μg cm^{-2} for Mn oxides and 91 μg cm^{-2} for Sibunit carbon. Currents were normalized to the geometric area of the electrode and were corrected to the background currents measured under a N_2 atmosphere. Insets: E_{mix} (V vs. RHE) as a function of the H_2O_2 concentration (*c*).

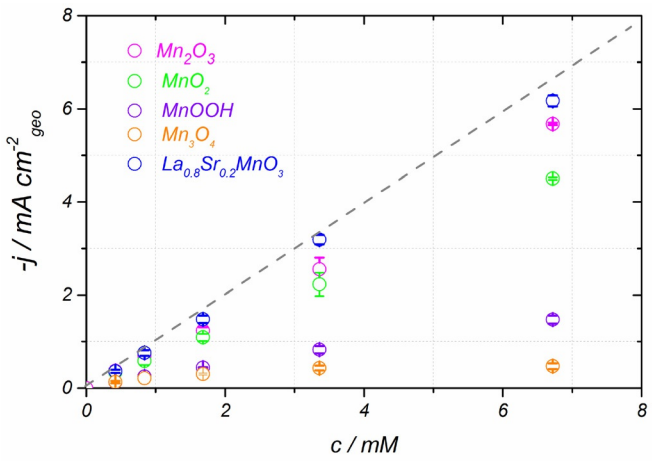

Figure 6. Influence of the H_2O_2 concentration (*c*) on the cathodic limiting currents measured for GC-supported thin films of Mn_2O_3_wet_3/C, MnOOH/C, Mn_3O_4/C, and $La_{0.8}Sr_{0.2}MnO_3$/C at 0.65 V vs. RHE and for MnO_2/C at 0.75 V vs. RHE in N_2-purged solutions of H_2O_2-containing 1 M NaOH at 900 rpm and 10 mV s^{-1}. Loadings were 91 μg cm^{-2} for manganese oxides and 91 μg cm^{-2} for Sibunit carbon. Dashed line shows the first-order concentration dependence for $La_{0.8}Sr_{0.2}MnO_3$.

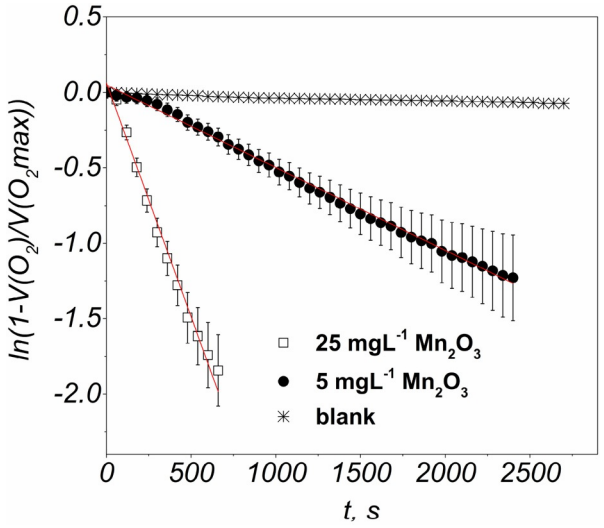

Figure 7. Evolution of $\ln[1-V(O_2)/V(O_2)_{max}]$ versus time in 0.99 mM aqueous H_2O_2 solution containing 5 (●) and 25 mg (□) of suspended Mn_2O_3_milled with a BET surface area of 8 $m^2 g^{-1}$. The results of a blank experiment in the absence of a catalyst are shown with crosses. Lines demonstrate linear fits.

tioning that the same (within experimental error) value of the catalytic hydrogen peroxide decomposition activity was found for Mn_2O_3 in an alkaline NaOH solution (see Table S2.3). Note also that Kanungo et al. investigated the pH dependence of the H_2O_2 decomposition activity of MnO_2 oxides with various crystalline structures and arrived at the conclusion that pH had a minor effect on the measured reaction rate constant.[28] The values of k_{het} found in this work are consistent with the literature data. For example, Soleymani et al.[25] for $La_{1-x}Ca_xMnO_3$ reported values of k_{het} between 5 and $7{\cdot}10^{-5}$ cm s^{-1}, similar to

Table 2. Selected experimental and simulated kinetic parameters for Mn oxides.

Material	Experimental data				Simulated parameters[a]			
	E_f[b] [V vs. RHE]	j_{ORR}[c] [μA cm^{-2}]	E_{mix}[d] [V]	k_{het}[e] [10^{-5} cm s^{-1}]	k_{het} [10^{-5} cm s^{-1}]	k_5 [s^{-1}]	k_2 [10^{13} cm^3 mol^{-1} s^{-1}]	k_3 [10^{10} s^{-1}]
Mn_2O_3	0.98	62	0.94	140 ± 20	230	50	1.5	5.1
$LaMnO_3$	0.92	9	0.94	9 ± 2	16	10	0.03	0.1
MnO_2	0.88	4	0.87	16 ± 2	20	2.0	0.3	1.0
MnOOH	0.88	1.7	0.84	3 ± 0.5	2	0.05	0.15	0.5

[a] For full set of parameters, see Section S3. [b] Formal potential of the $Mn^{IV/III}$ transition of surface cations determined from the CV curves in 1 M NaOH. For further details, see Ref. [16]. [c] Kinetic ORR currents at 0.9 V normalized to the BET surface areas of the oxides reproduced from Ref. [16] and determined from the RDE voltammograms measured in O_2-saturated 1 M NaOH electrolyte at 25 °C. [d] Here and in what follows the values of the mixed potential refer to the positive scans of the RDE voltammograms acquired in 1 M NaOH + 0.84 mM H_2O_2 at 900 rpm. Note that the value of the mixed potential is also sensitive to the specific surface area of the oxide due to the ORR contribution to the cathodic branch (see Ref. [15]). [e] Heterogeneous rate constant for the decomposition of H_2O_2 determined in aqueous solutions of 0.99 mM H_2O_2.

the values found in this work for Mn perovskites (Table 2 and Table S2.3).

Despite numerous studies, the mechanism of H_2O_2 decomposition is not fully understood, and a large variety of pathways have been proposed for different catalysts. Some authors suggest that H_2O_2 decomposition occurs through a chemical pathway,[29,30,31] whereas others believe that the decomposition reaction is the sum of the electrochemical reduction and oxidation of H_2O_2.[32,33] Both likely involve the redox transition of the metal cation.[21–26,31,33,34]

2.4. Comparison of the Oxygen Reduction and Hydrogen Peroxide Reactions: Experiment versus Kinetic Modeling

In this section, we compare experimentally obtained data with the simulations. Whereas the previous version of our microkinetic model was set up to reproduce exclusively the ORR activity of the Mn oxides and to explain its correlation with the formal potential of the surface Mn^{IV}/Mn^{III} redox transition, in this work we consider the three groups of experimental data, namely, 1) the RDE voltammograms for the HPRR/HPOR, 2) the catalytic decomposition of hydrogen peroxide, and 3) the RDE voltammograms for the ORR for various Mn oxides in a large interval of variable parameters (concentrations, rotation rates). The kinetic modeling aims at verifying the consistency of the proposed mechanism with the whole set of experimental data and at identifying the main elementary reaction steps that determine the ORR and hydrogen peroxide activities of various Mn oxides. It has to be stressed that the assumptions used in the model and the numerous unknown rate constants prevent us from quantitative determination of the rate constant values by fitting the current potential curves. The values of k_{het} and of other kinetic constants were adjusted to reproduce the main features of the three groups of experimental data.

Briefly, the simulations were performed as follows: rate constants of step 1, k_1 and k_{-1}, were adjusted to reproduce the formal potential E_f of the Mn^{IV}/Mn^{III} redox transition (for determination of E_f from the CV curves in N_2-purged 1 M NaOH electrolyte, see Ref. [16]). To reproduce the qualitative shape of the CV curves, a Frumkin isotherm with a repulsive interaction parameter $\gamma = 6$ was chosen. However, the main conclusions of this work are not affected by the value of γ (for comparison, the simulated current–potential curves performed for $\gamma = 0$ are shown in Figure S3.1). H_2O_2 decomposition was considered as a sum of electrochemical oxidation and electrochemical reduction reactions. The rate constants k_2, k_3, k_{-2}, and k_{-3} were adjusted to reproduce simultaneously the experimental data for the onset of the ORR current, the value of E_{mix}, and the value of k_{het}. Note that the ratios k_2/k_{-2} and k_3/k_{-3} were fixed to account for the standard potential of the O_2/HO_2^- redox couple [see. Eq. (2)]. The rate constant k_5 was chosen to reproduce the value of k_{het} and of the HPRR limiting current for MnOOH and MnO_2. Selected rate constants are shown in Table 2, whereas the full set of parameters entering the simulations is given in Section S3.

Experimental RDE current potential curves acquired in N_2-purged 1 M NaOH containing 0.84 mM HO_2^- (this work) and in O_2-saturated 1 M NaOH (Ref. [16]) for MnOOH, MnO_2, Mn_2O_3, and $LaMnO_3$ are compared with the simulated ones in Figure 8. For Mn_3O_4, we did not manage to find a unique set of parameters for the description of the ORR and HPOR/HPRR. As mentioned above, this might be related to the degradation of the Mn_3O_4 surface in the presence of hydrogen peroxide (see Figure S1.1).

The current–potential curves for the MnOOH/C electrodes, which demonstrate the lowest catalytic activity either in the ORR or in the decomposition of H_2O_2, are shown in Figure 8a, b. The characteristic features of MnOOH are low (inferior to the diffusion-controlled) HPRR and ORR currents at high cathodic overpotentials. The value of E_{mix} of the MnOOH/C electrode takes a value of around 0.84 V versus RHE, significantly below that of either Pt/C or other Mn oxides (see Table 2 and Figure 8c, e), which suggests that the kinetics of the HPRR [Eq. (3)] on MnOOH are slower than those of the HPOR counterpart [Eq. (2)]. By choosing a small rate constant for chemical step 5 (k_5), the kinetic model was able to reproduce the main features of the current–potential curves and the low value of k_{het}. It is the small value of k_5 that is responsible for the rotation-rate independence of the cathodic limiting current in the presence of HO_2^- for MnOOH/C (see Figures 3 and 4). Notably, the onset of the ORR on MnOOH is 40 mV higher than the value of E_{mix}. This could be reproduced by simulations

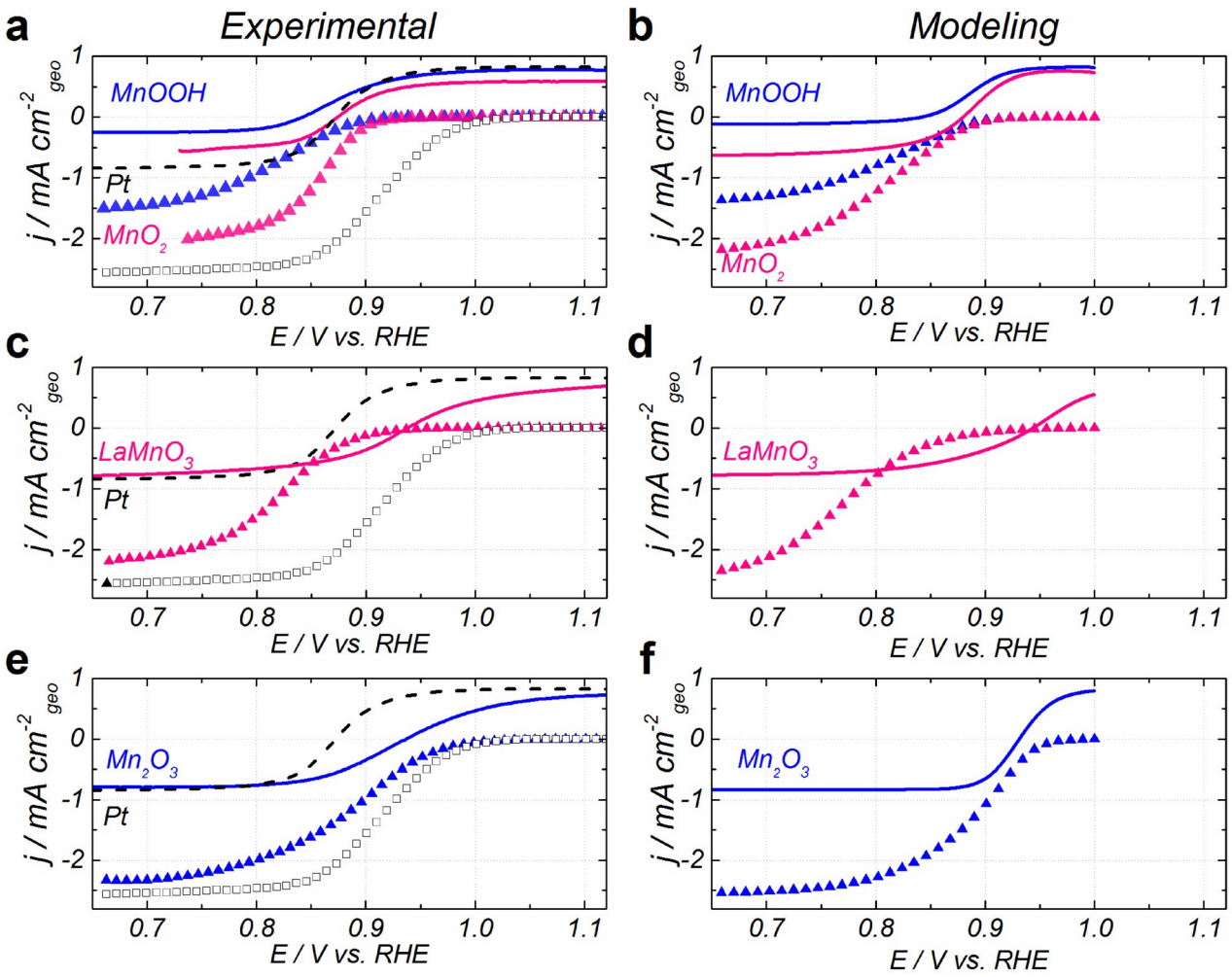

Figure 8. a, c, e) Experimental at 900 rpm and 10 mV s^{-1} and b, d, f) simulated RDE voltammograms in N_2-purged 1 M NaOH + 0.84 mM H_2O_2 (solid lines) and O_2-saturated 1 M NaOH (triangles) for GC-supported thin films of MnOOH/C, MnO_2/C, $LaMnO_3$/C, and Mn_2O_3_wet_3/C. Catalyst loadings were 91 μg cm^{-2} manganese oxide + 91 μg cm^{-2} Sibunit carbon. Experimental RDE voltammograms were normalized to the electrode geometric area and were corrected to the background currents measured under the N_2 atmosphere. Simulations were performed for the Frumkin interaction parameter $\gamma = 6$ and kinetic rate constants presented in Table 2 and Table S3.1. RDE curves for Pt/C in 1 M NaOH + 0.84 mM H_2O_2 (dashed lines) and O_2-saturated 1 M NaOH (empty squares) are replotted from Ref. [15] for comparison.

performed within the mechanism displayed in Figure 1. In the potential interval between E_{mix} and the onset of the ORR, the sign of the overall current (cathodic vs. anodic) is determined by the relative concentrations of O_2 and HO_2^- in solution. In the absence of O_2 in the electrolyte (N_2-purged solution) containing 0.84 mM HO_2^-, the current in this potential interval is positive, which suggests that the oxidation of HO_2^- [Eq. (−2)] is faster than the reduction of O_2 to HO_2^- [Eq. (2)], whereas in an O_2-saturated electrolyte the reduction of O_2 into HO_2^- [Eq. (2)] is predominant and the overall current is negative. For MnOOH, one of the major factors limiting the ORR activity and the decomposition of hydrogen peroxide is the slow HPRR kinetics (slow chemical step 5 responsible for the reaction-limited HPRR current at high cathodic overpotentials).

Data for MnO_2/C are also shown in Figure 8 a, b. Kinetic modeling suggests that the rate constants for steps 2 and 3 for MnO_2 are about 2 times higher than those for MnOOH, whereas the rate constant for chemical step 5 for MnO_2 is about 40 times higher than that for MnOOH. Given that the HPRR is faster on MnO_2 than on MnOOH, the value of E_{mix} is positively shifted by around 30 mV and the kinetic current for the ORR at 0.9 V is increased approximately 2.4-fold (Table 2).

The Mn perovskite/C (both $LaMnO_3$ and $La_{0.8}Sr_{0.2}MnO_3$) electrodes (Figure 8 c, d) exhibit significantly different features than the MnOOH electrode. In H_2O_2-containing solutions, the diffusion limiting currents are reached for both the HPRR (cathodic branch) and the HPOR (anodic branch), and E_{mix} is equal to 0.94 V versus RHE. The value of E_{mix} is shifted in the positive direction relative to the values of E_{mix} for MnOOH and MnO_2, and this points to faster HPRR kinetics but also to slower HPOR kinetics on the Mn perovskites. To account for the experimental observations within the same reaction mechanism, one has to assume a high value of k_5 (responsible for the diffusion-limited HPRR at 0.65 V vs. RHE) but low values of the rate constants

for steps 2 and 3 (largely responsible for the positive shift in E_{mix}). By assuming a significant increase in the rate constant for step 5 (relative to that for either MnOOH or MnO_2) and a decrease in the rate constants for steps 2 and 3 (Table 2), the model was able to reproduce the experimental data for the HPRR/HPOR and the ORR (Figure 8d), including the position of the ORR onset, which on Mn perovskites was slightly below E_{mix}. Thus, for Mn perovskites the main factor limiting their ORR activity seems to be the slow kinetics of the steps responsible for the conversion of O_2 into H_2O_2 and back (steps 2 and 3 in Figure 1). It is interesting that despite the slow kinetics of steps 2 and 3, the overall ORR rate on Mn perovskites is enhanced relative to that of either MnOOH or MnO_2 by the fast HPRR kinetics (fast step 5).

Let us now turn to Figure 8e,f. In comparison to other Mn oxides, the Mn_2O_3/C electrode exhibits high activity either in the HPRR or in the ORR. Nevertheless, the ORR activity of Mn_2O_3 is slightly inferior to that of Pt and may be due to a slower HPOR on Mn_2O_3 (see the positive shift in the E_{mix} value for Mn_2O_3 relative to that for Pt/C). It is worth comparing the magnitudes of the gaps between the ORR onset potentials and the values of E_{mix} for Pt/C and Mn_2O_3/C. One can see that the ORR onset potential for Pt/C is roughly 120 mV higher than the E_{mix} value. At potentials positive of E_{mix}, once HO_2^- is formed by O_2 reduction, it will be oxidized back into O_2. The occurrence of the ORR in the potential interval above E_{mix} is explained by the so-called "direct" (without formation of the peroxide intermediate) ORR pathway on Pt. According to Ruvinskiy et al.,[35] the ORR on Pt nanoparticles follows a direct pathway at potentials close to the ORR onset, whereas at lower potentials the ORR occurs through the hydrogen peroxide intermediate. For Mn_2O_3/C, the value of E_{mix} is also higher than the ORR onset potential, but only by about 50 mV. Such a difference between the value of E_{mix} and the ORR onset can be reproduced even within the $2e^- + 2e^-$ "series" ORR mechanism. Although at this stage it is not possible to prove unambiguously the occurrence of the "direct" ORR pathway for Mn_2O_3, this pathway might be responsible for the different slopes of the simulated and experimental voltammograms in the HO_2^--containing electrolyte (see Figure 8e,f).

In summary, kinetic modeling reveals that the different behaviors of the Mn oxides in the ORR and hydrogen peroxide reaction cannot be fully accounted for by the influence of the potential of the redox transition of the surface cations, E_f, but requires considering the effects of structure/composition on the rate constants of the elementary steps (Table 2). One may notice that k_5 scales with the redox potential of the $Mn^{IV/III}$ transition more or less the same way as the ORR activity ($Mn_2O_3 > LaMnO_3 > MnO_2 > MnOOH$), likely because of the involvement of this redox transition in step 5 (Figure 1). However, the rate constants of steps 2 and 3, which involve substitution of a hydroxo group by molecular oxygen accompanied by electron and proton transfer, scale differently, namely, $Mn_2O_3 > MnO_2 > MnOOH > LaMnO_3$. Note that in our model, rate constants for steps 2 and 3 are not independent and have to be considered together, so it is not surprising that they increase and decrease concomitantly. Surprising is that MnOOH, which is much less active than the Mn perovskites in the ORR, demonstrates higher rate constants for steps 2 and 3.

It would be tempting to bridge the detected differences in the rate constants with the crystal structures of the Mn oxides. Whereas precise understanding of the relationships between the structure and composition, on the one hand, and surface reactivity, on the other hand, certainly requires extensive computational work, it is worth identifying an integral structural parameter that varies within the set of investigated oxides and could potentially be responsible for the observed behavior. The observed steep changes in k_2/k_3 are hard to explain by minor variations in the Mn–O distances in the studied oxides (see Section S6). The integral structural parameter, which changes drastically and concomitantly with k_2 and k_3, is the oxygen coordination number (i.e. the number of O–Mn bonds per lattice O). Indeed, in the $LaMnO_3$ structure the O ion is bonded to two cations, in MnO_2 and MnOOH the O ion is bonded to three cations, and in Mn_2O_3 the O ion is bonded to four Mn cations. If the structure is terminated at the surface, the actual number of bonds might change, but this trend is likely to remain. The differences in the oxygen ion coordination number likely affect the strength of water bonding (and thus the surface acidity) and probably also O_2 bonding to the oxide surface, which thus influences the rates of steps 2 and 3. It is well established that along with redox, the acid–base properties of transition-metal oxides are essential for their catalytic activity (see Ref. [36] and references cited therein). Note that protons on the oxide surfaces strongly influence molecular oxygen bonding.[37] One may thus tentatively attribute the extraordinary ORR activity of Mn_2O_3 in the series of investigated Mn oxides to a favorable combination of its redox and acid–base properties. To obtain further insight into the nature and rate constants of the elementary steps and into their dependence on the surface structure and composition of transition-metal oxides (including the coordination numbers of the surface anions and cations), ab initio calculations are required, which are underway.

3. Conclusions

In this work, we studied the catalytic and electrocatalytic reactions of hydrogen peroxide on a set of Mn oxides with the objective to obtain further insight into the mechanism of the ORR. Apparently, all of the investigated Mn oxides showed noticeable activity in the hydrogen peroxide reactions, and Mn_2O_3 oxide was the most active, whereas MnOOH was the least active. Three groups of experimental data, 1) the RDE voltammograms for hydrogen peroxide oxidation/reduction, 2) the heterogeneous rate constant (k_{het}) for the catalytic decomposition of hydrogen peroxide, and 3) the RDE voltammograms for the ORR (data from Ref. [16]), were compared and analyzed with the help of a microkinetic model in a self-consistent manner.

We concluded that the ORR activity of the Mn oxides may be reasonably explained within the "series" $2e^- + 2e^-$ pathway. The choice of the model parameters allowed us to reproduce the order of magnitude of the heterogeneous rate constant

(k_{het}) for the decomposition of hydrogen peroxide and most of the experimental features of the current–potential curves for Mn_2O_3, Mn perovskites, MnO_2, and MnOOH. Clearly, to be capable of catalyzing the ORR through a "series" mechanism, the Mn oxides must be active both in the reduction of O_2 to H_2O_2 and in the reduction of H_2O_2 to water (OH^-). By combining experiments and modeling we were able to conclude that Mn_2O_3 was characterized by high catalytic activity for both the reduction of O_2 to hydrogen peroxide and subsequent reduction of the latter to water. The other extreme case was exhibited by MnOOH, which showed the lowest activity both in the ORR and in the hydrogen peroxide reactions. The main factor limiting the ORR activity of MnOOH seemed to be its low activity in the reduction of hydrogen peroxide. Moreover, the ORR activity of the Mn perovskites was rather limited by the slow transformation of O_2 into the H_2O_2 intermediate, whereas its subsequent reduction was found be fast. The ORR catalysis of the Mn oxides was found to be related to the surface redox potential of the Mn cations and (tentatively) to the coordination numbers of the surface anions, the latter likely affecting the acid–base properties of the surface and molecular oxygen bonding.

Acknowledgements

The authors thank P. Simonov of the Boreskov Institute of Catalysis (Novosibirsk, Russia) for supplying Sibunit Carbon and the Tokuyama Company for supplying the alkaline ionomer. Financial support received within ERA.NET.RUS.PLUS project (#270 NANO-Morf), Région Alsace, and the French Ministry of Foreign Affairs for a scholarship to A.R. is gratefully appreciated.

Keywords: crystal structure · manganese oxides · oxygen · hydrogen peroxide · reduction

[1] Z. Zhang, J. Liu, J. Gu, L. Su, L. Cheng, *Energy Environ. Sci.* **2014**, *7*, 2535.
[2] F. Chen, J. Chen, *Chem. Soc. Rev.* **2012**, *41*, 2172.
[3] J. W. D. Ng, Y. Gorlin, T. Hatsukade, F. T. Jaramillo, *Adv. Energy Mater.* **2013**, *3*, 1545.
[4] M. T. M. Koper, *J. Electroanal. Chem.* **2011**, *660*, 254 – 260.
[5] Y. J. Wang, J. Qiao, R. Baker, J. Zhang, *Chem. Soc. Rev.* **2013**, *42*, 5768.
[6] W. T. Hong, M. Risch, K. A. Stoerzinger, A. Grimaud, J. Suntivich, Y. Shao-Horn, *Energy Environ. Sci.* **2015**, *8*, 1404 – 1427.
[7] Q. He, E. J. Cairns, *J. Electrochem. Soc.* **2015**, *162*, F1504 – F1539.
[8] K. A. Stoerzinger, M. Risch, B. Han, Y. Shao-Horn, *ACS Catal.* **2015**, *5*, 6021 – 6031.
[9] L. Q. Mao, D. Zhang, T. Sotomura, K. Nakatsu, N. Koshiba, T. Ohsaka, *Electrochim. Acta* **2003**, *48*, 1015 – 1021.
[10] R. B. Valim, M. C. Santos, M. R. V. Lanza, S. A. S. Machado, F. H. B. Lima, M. L. Calegaro, *Electrochim. Acta* **2012**, *85*, 423 – 431.
[11] A. Bonakdarpour, M. Lefevre, R. Yang, F. Jaouen, T. Dahn, J. P. Dodelet, J. R. Dahn, *Electrochem. Solid-State Lett.* **2008**, *11*, B105 – B108.
[12] M. Inaba, H. Yamada, J. Tokunaga, A. Tasaka, *Electrochem. Solid-State Lett.* **2004**, *7*, A474 – A476.
[13] D. Dobos, *Electrochemical Data*, Akademiai Kiado, Budapest, **1978**.
[14] T. Poux, A. Bonnefont, G. Kéranguéven, G. A. Tsirlina, E. R. Savinova, *ChemPhysChem* **2014**, *15*, 2108 – 2120.
[15] T. Poux, A. Bonnefont, A. Ryabova, G. Kéranguéven, G. A. Tsirlina, E. R. Savinova, *Phys. Chem. Chem. Phys.* **2014**, *16*, 13595—13600.
[16] A. S. Ryabova, F. S. Napolskiy, T. Poux, S. Y. Istomin, A. Bonnefont, D. M. Antipin, A. Y. Baranchikov, E. E. Levin, A. M. Abakumov, G. Kéranguéven, E. V. Antipov, G. A. Tsirlina, E. R. Savinova, *Electrochim. Acta* **2016**, *187*, 161 – 172.
[17] T. Poux, F. S. Napolskiy, T. Dintzer, G. Kerangueven, S. Y. Istomin, G. A. Tsirlina, E. V. Antipov, E. R. Savinova, *Catal. Today* **2012**, *189*, 83 – 92.
[18] V. Rao, P. A.. Simonov, E. R. Savinova, G. V. Plaksin, S. V. Cherepanova, G. N. Kryukova, U. Stimming, *J. Power Sources* **2005**, *145*, 178 – 187.
[19] J. Deren, J. Haber, A. Podgorecka, J. Burzyk, *J. Catal.* **1963**, *2*, 161 – 175.
[20] T. Minami, P. Ravindranathan, K. C. Patil, *Proc. Indian Acad. Sci.* **1987**, *99*, 209 – 215.
[21] A. Ariafard, H. R. Aghabozorg, F. Salehirad, *Catal. Commun.* **2003**, *4*, 561 – 566.
[22] H. Falcón, R. E. Carbonio, *J. Electroanal. Chem.* **1992**, *339*, 69 – 83.
[23] H. Falcón, R. E. Carbonio, J. L. G. Fierro, *J. Catal.* **2001**, *203*, 264 – 272.
[24] J. A. Alonso, M. J. Martinez-Lope, H. Falcon, R. E. Carbonio, *Phys. Chem. Chem. Phys.* **1999**, *1*, 3025 – 3030.
[25] M. Soleymani, A. Moheb, D. Babakhani, *Chem. Eng. Technol.* **2011**, *34*, 49 – 55.
[26] H. Yang, T. Zhang, H. Tian, J. Tang, D. Xu, W. Yang, L. Lin, *React. Kinet. Catal. Lett.* **2001**, *73*, 311 – 316.
[27] Y. N. Lee, R. M. Lago, J. L. G. Fierro, J. Gonzalez, *Appl. Catal. A* **2001**, *215*, 245 – 256.
[28] S. B. Kanungo, K. M. Parida, B. R. Sant, *Electrochim. Acta* **1981**, *26*, 1157 – 1167.
[29] F. Jaouen, *J. Phys. Chem. C* **2009**, *113*, 15433 – 15443.
[30] C. M. Lousada, A. J. Johansson, T. Brinck, M. Jonsson, *J. Phys. Chem. C* **2012**, *116*, 9533 – 9543.
[31] S. S. Lin, M. D. Gurol, *Environ. Sci. Technol.* **1998**, *32*, 1417 – 1423.
[32] R. Venkatachalapathy, G. P. Davila, J. Prakash, *Electrochem. Commun.* **1999**, *1*, 614 – 617.
[33] D. Fu, P. G. Keech, D. W. Shoesmith, J. C. Wren, *Electrochim. Acta* **2010**, *55*, 3787 – 3796.
[34] F. C. C. Moura, M. H. Araujo, J. D. Ardisson, W. A. A. Macedo, A. S. Albuquerque, R. M. Lago, *J. Braz. Chem. Soc.* **2007**, *18*, 322 – 329.
[35] P. S. Ruvinskiy, A. Bonnefont, C. Pham-Huu, E. R. Savinova, *Langmuir* **2011**, *27*, 9018 – 9027.
[36] I. E. Wachs, *Catal. Today* **2005**, *100*, 79 – 94.
[37] L. L. Liu, Q. Liu, Y. P. Zheng, Z. Wang, C. X. Pan, W. Xiao, *J. Phys. Chem. C* **2014**, *118*, 3471 – 3482.

Manuscript received: May 7, 2016
Accepted Article published: July 13, 2016
Final Article published: August 2, 2016